Title

Numerical analysis of experimental studies of methane hydrate dissociation induced by depressurization in a sandy porous medium

Authors

Yin, Zhenyuan
Moridis, George
Chong, Zheng Rong
et al.

Publication Date

2018-11-01

DOI

10.1016/j.apenergy.2018.08.115

Peer reviewed

Numerical analysis of experimental studies of methane hydrate dissociation induced by depressurization in a sandy porous medium

Zhenyuan Yin[ab] George Moridis[cda] Zheng Rong Chong[a] Hoon Kiang Tan[b] Praveen Linga[a]

Abstract

Methane Hydrates (MHs) are a promising energy source abundantly available in nature. Understanding the complex processes of MH formation and dissociation is critical for the development of safe and efficient technologies for energy recovery. Many laboratory and numerical studies have investigated these processes using synthesized MH-bearing sediments. A near-universal issue encountered in these studies is the spatial heterogeneous hydrate distribution in the testing apparatus. In the absence of direct observations (e.g. using X-ray computed tomography) coupled with real time production data, the common assumption made in almost all numerical studies is a homogeneous distribution of the various phases. In an earlier study (Yin et al., 2018) that involved the numerical description of a set of experiments on MH-formation in sandy medium using the excess water method, we showed that spatially heterogeneous phase distribution is inevitable and significant. In the present study, we use as a starting point the results and observations at the end of the MH formation and seek to numerically reproduce the laboratory experiments of depressurization-induced dissociation of the spatially-heterogeneous MH distribution. This numerical study faithfully reproduces the geometry of the laboratory apparatus, the initial and boundary conditions of the system, and the parameters of the dissociation stimulus, capturing accurately all stages of the experimental process. Using inverse modelling (history-matching) that minimized deviations between the experimental observations and numerical predictions, we determined the values of all the important flow, thermal, and kinetic parameters that control the system behaviour, which yielded simulation results that were in excellent agreement with the measurements of key monitored variables, i.e. pressure, temperature, cumulative production of gas and water over time. We determined that at the onset of depressurization (when the pressure drop – the driving force of dissociation – is at its maximum), the rate of MH dissociation approaches that of an equilibrium reaction and is limited by the heat transfer from the system surroundings. As the effect of depressurization declines over time, the dissociation reaction becomes kinetically limited despite significant heat inflows from the boundaries, which lead to localized temperature increases in the reactor.

Keywords: Methane hydrate, Depressurization, Kinetic reaction, Sandy porous medium, Heterogeneous, TOUGH+Hydrate v1.5

1. Introduction

1.1. Background

Gas hydrates are solid crystalline compounds, which consist of gas molecules (called “guests”) that are trapped in a crystal lattice formed by water molecules. Typical guest gases are hydrocarbons with low molecular weight (e.g. CH_4, C_2H_6, C_3H_8), as well as other gases like CO_2, N_2 and H_2S [1]. Depending on the attributes of the gas molecules, three primary hydrate structures have been identified, namely structure I (sI), structure II (sII) and structure H (sH) [2]. If the hydrate-forming gas is pure CH_4, the resulting methane-hydrate (MH) crystals have a sI structure, with two 5^{12} small cages and six $5^{12}6^2$ large cages. MH is thermodynamically stable under favourable low temperature (T) and high pressure (P) conditions.

MH occur abundantly (~20,000 TCM [3], [4] in nature at (a) appropriate permafrost locations and (b) in oceanic deposits at and below the seafloor near the continental shelf [5]. The amount of CH_4 trapped in MH is vast, possibly twice as large as the equivalent of the combined world reserves of oil and gas [6]. An important feature of MH is that it has a high energy storage capacity: upon dissociation, 1 m^3 of MH releases 164 m^3 of CH_4 under STP condition [7]. Because of these reasons, MH is being considered as a potential future energy resource, and as such it has become the focus of considerable attention in several recent studies conducted by several countries (USA, Canada, Japan, S. Korea, China, India, Singapore, etc.).

Four different methods have been proposed so far to produce CH_4 gas from hydrates: thermal stimulation, depressurization, the use of inhibitors and gas exchange [6]. The working principle of these methods is based on (a) altering the reservoir P/T condition to a region outside the MH stability zone, or (b) by shifting the hydrate equilibrium curve away from the original MH stability region [8]. A number of field tests have been carried out to investigate the technical feasibility of recovering CH_4 gas from hydrate reservoir at both permafrost [9], [10], [11] and marine locations [12]. A summary of these field tests, of the associated production methods and of the corresponding production rates are summarized in Table 1. Under the conditions of the limited-duration field tests conducted thus far, the gas production rate from hydrate deposits has not yet reached the level of economic viability of conventional gas reservoirs (which is considered to be on the scale of 100,000 m^3/day [13], but the production of gas from hydrates have been exhibiting a consistent (and promising) upward trend. Although considerable progress has been attained on the subject of gas production from natural hydrate deposits, technical challenges still remain in the areas of well design and completion, sand production and control, and optimization of fluids production [14].

Table 1. Summary of gas hydrate filed production tests.

Site (Location)	Time	Method	Production duration (day)	Cumulative gas production volume (m^3)	Average gas production rate (m^3/day)
	Mar 2002	Thermal Stimulation [9]	5	515	103
Mallik (Permafrost)	Apr 2007	Depressurization [74]	1	830	830
	Mar 2008	Depressurization [74]	5.5	13,200	2400
Ignik Sikumi (Permafrost)	May 2012	Injection of $CO_2$and $CO_2 + N_2$[11]	38	24,210	637
	Jan 2013	Depressurization [12]	6	120,000	20,000
Nankai Trough (Marine)	April 2017	Depressurization [75]	12	35,000	2917
	June 2017	Depressurization [75]	24	200,000	8333
Shenhu Area (Marine)	May 2017	Depressurization [76]	60	300,000	5000

Lack of knowledge on significant parameters that define key hydrate properties and behaviour, coupled with the limited number of field tests (which could provide some answers) and the significant challenges encountered in these field explorations [15], necessitate the study of MH-bearing sediments (an analogue of natural hydrate-bearing geologic media) under controlled laboratory conditions. Of particular interest is the investigation on the kinetic (dynamic) behaviour of MH formation and dissociation, as well as the associated behaviour of the reservoir fluids under a variety of conditions and flow regimes [16], [17], [18], [19], [20], [21]. A common limitation of these studies is that hydrate saturation is estimated based on the measurement of P and T in the reactor on a bulk basis, without consideration of its spatial variability.

Recently, a variety of techniques have been applied in laboratory studies of MH formation and dissociation experiments in order to quantify the spatial distributions of in-situ phase saturations, mainly those of the hydrate phase (S_H) and of the aqueous phase (S_A). In-situ observations of S_A during MH-dissociation under varying back-pressures were carried out using Magnetic Resonance Imaging (MRI) techniques [22]. This study determined that MH dissociation propagates radially inside a cylindrical testing apparatus, and that the resulting S_A is spatially heterogeneous during dissociation. The same MRI technique was applied to investigate gas production under different

initial S_A conditions [23], [24], and revealed that (a) higher S_A occurs at the centre of the reactor after hydrate formation, and (b) that the heterogeneous water saturation (with high S_A at the vessel bottom) impedes gas production during depressurization-induced dissociation. A more direct measurement on the spatial distribution of S_H using MRI was carried out by Birkedal et al. [25]. This study indicates that higher saturation of S_H is present in the vicinity of the end-piece of the vessel, while higher concentrations of S_G is located at outer radial positions with significant excess water in the middle segment of the core. Similar MRI findings of spatially heterogeneous hydrate distribution was also reported in a study of MH formation in a silica sand bed inside a millimetre-scale reactor [26].

Besides MRI, X-ray Computed Tomography (CT) also demonstrated its ability to track $S_H$both spatially and temporally in a number of formation and dissociation studies on (a) hydrate cores extracted from natural field deposits [27], [28], [29] and (b) hydrate-bearing sediments synthesized in the laboratory [30], [31], [32], [33], [34]. These studies have provided visual evidence that the S_H distribution in the samples is not uniform because of the uneven distribution and migration of water under gravity and capillary effect during hydrate formation [32]. Electrical Resistivity Tomography (ERT) is another experimental technique that has been used to describe the S_H spatial distribution in reactors. In their study of MH formation and dissociation behaviour in a meter-scale reactor, Priegnitz et al. [35], [36] indicated that localized S_H can deviate significantly from the bulk saturation estimate (computed for the entire reactor). These earlier experimental studies have consistently provided strong evidence on the nature of spatially heterogeneous S_H in laboratory apparatus.

In addition to experimental studies, a number of simulation studies have been carried out to model the behaviour of hydrate dissociation and fluids production in laboratory-scale systems. Masuda et al. [37] used a 1D numerical model to reproduce laboratory experiments involving gas and water production during MH dissociation in Berea sandstone cores. His numerical model coupled the kinetic model of hydrate dissociation proposed by Kim et al. [38] with the standard equations of flow of fluids and heat in porous media. His model could not accurately reproduce their experimental observations. This was attributed to the fact that S_H was not uniformly formed in the core before the onset of depressurization, thus leading to discrepancies between the simulated and the measured T in the core. A number of more recent simulation studies [39], [40], [41], [42], [43] that analysed the same set of experiments led to improved matches of measurements and predictions of P, T and of the cumulative gas production (V_T) by implementing representative boundary conditions (i.e., an adiabatic boundary [41], a constant heat flux boundary [39], [43] and a constant T boundary [40], [42]and more reliable constitutive relationships (i.e., a permeability reduction model [43], a relative permeability model [41], and a

kinetic rate model [39]. However, despite the improvements, discrepancies (sometimes significant) continued to exist.

A consistent limitation of these studies is the assumption of a homogeneous initial spatial distribution of the various phases ($S_H = 46.5\%$ and $S_A = 35.1\%$) in the reactor vessel before hydrate dissociation, which undermined the validity of the simulation approach and their predictability. This limitation has not been well discussed so far in the literature for a number of reasons: (a) the method of the MH formation used in the Masuda's experiment was not well documented [44] and (b) the complexity (occasionally overwhelming) often encountered in simulating the dynamic behaviour of hydrate formation in a laboratory apparatus, and the associated numerical convergence issues [25], [45], [46], [47]. Practically all numerical studies simulating the behaviour of hydrate dissociation and fluid production have been conducted based on the simplifying assumption (approximation) of an initial spatially homogeneous hydrate distribution [48], [49], [50], [51], and very few have addressed the issue of heterogeneity [52].

The issue of heterogeneity in the spatial distribution of S_H in an experiment of hydrate dissociation was suggested in the numerical study of Yin et al. [53] that modelled a set of earlier laboratory studies of thermally-induced dissociation [54]. Based on the deviations between the simulated- and measured-T over time at different thermocouple positions and the inability to reconcile the two using the outer limits of the range of realistic thermal properties, Yin et al. [53] reached the conclusions (a) that the assumption of an equilibrium model describing the dissociation reaction was invalid as it resulted in an inordinately fast gas production rate that could not be retarded by any combination of even unrealistic thermal property values, and (b) that the laboratory observations could only be explained by a kinetic dissociation reaction, and (c) a heterogeneous S_H distribution.

In their subsequent study, Yin et al. [55] addressed these issues by reproducing faithfully and numerically all the steps of the laboratory study of Chong et al. [19], [54], beginning with the multi-step hydrate formation in a sandy medium using the excess-water approach and fully accounting for the spatial heterogeneity. Given the limited volume of the reactor and the high permeability of the sand in the experiment, they concluded that hydrate formation was predominantly controlled by thermal processes, and that uniformity of the initial phase saturation appeared to be nearly impossible because of gravity, capillary effects and the reactor geometry. The very good agreement of laboratory observations and numerical predictions confirmed both the kinetic nature of the hydrate reaction in the experimental studies, and the heterogeneity in the spatial distribution of various phases during the various steps of hydrate formation and redistribution. The study of Yin et al. [55] provided the heterogeneous phase saturation distributions at the end of the hydrate formation process, which are used as the initial conditions (a key input) in the current study of hydrate dissociation (thus completing the

numerical representation of the earlier laboratory study of hydrate formation and dissociation [19], [54].

1.2. Objectives

The main objective of this study is to numerically reproduce and analyse the 2nd phase of the earlier laboratory experiment of Chong et al. [19], which involves the depressurization-induced dissociation of the heterogeneous hydrate sample formed by the excess-water method in a reactor. As already discussed, the initial phase saturations in this study were provided by the work of Yin et al. [55]. By minimizing the deviations between experimental measurements and numerical predictions, we seek to numerically duplicate the P, T, the cumulative gas production volume (V_G) and the cumulative water production mass (V_A) observed during the depressurization phase of the earlier study [19], and to determine through inverse modelling (history-matching) the values of important parameters that control the process. Note that the inverse modelling (history-matching) process in the precursor study has already provided optimized values for a set of important parameters [55], thus limiting the number of parameters that need to be optimized in the current study. Additionally, we seek to obtain a deeper understanding of the overall behaviour of the dissociating system by monitoring the evolution of various key variables (P, T, S_A, S_G and S_H) over time during the depressurization process.

2. The underlying laboratory studies of MH dissociation

In this section, we present a summary of the laboratory studies that provided the data for our numerical analysis. The interested reader is directed to the study of Chong et al. [19] for a detailed description of the associated experimental study on the depressurization- induced MH dissociation.

2.1. Experimental apparatus and materials

Fig. 1 shows a schematic of the entire experimental apparatus used in the laboratory study of Chong et al. [19] of MH formation and dissociation. The reactor geometry and configuration have been discussed in detail in our earlier publications of the MH formation experiment [19], [53], [54], and are summarized in Table 2 and shown in Fig. 2.

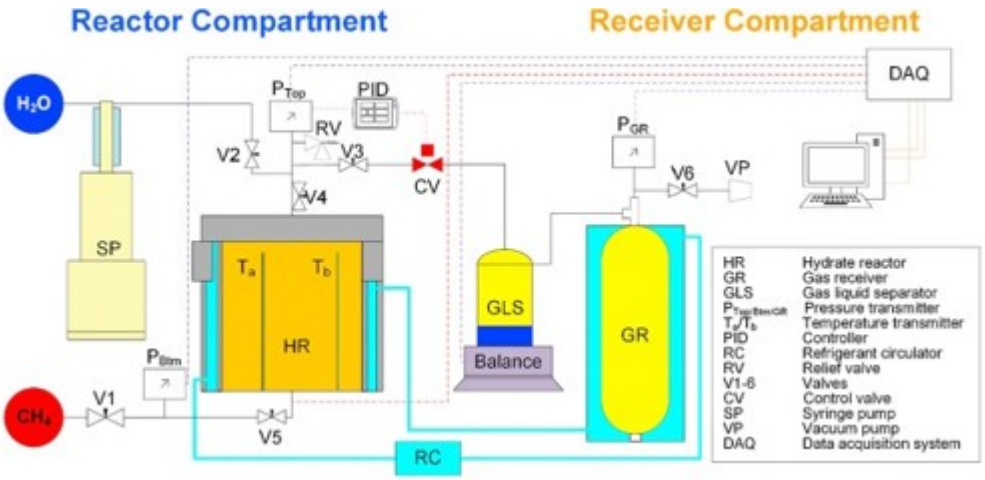

Fig. 1. Schematic of the experimental apparatus for MH formation and dissociation experiment.

Table 2. Geometry of the reactor used in the methane hydrate formation and dissociation experiment.

Parameter	**Value**
Internal height of reactor	120.0 mm
Internal diameter of reactor	102.0 mm
Internal volume of reactor	0.98 L
Thickness of reactor wall	15.0 mm
Thickness of reactor top and bottom	25.0 mm
External diameter of pressure outlet	9.52 mm
Internal diameter of pressure outlet	4.60 mm
Material of reactor	SS316

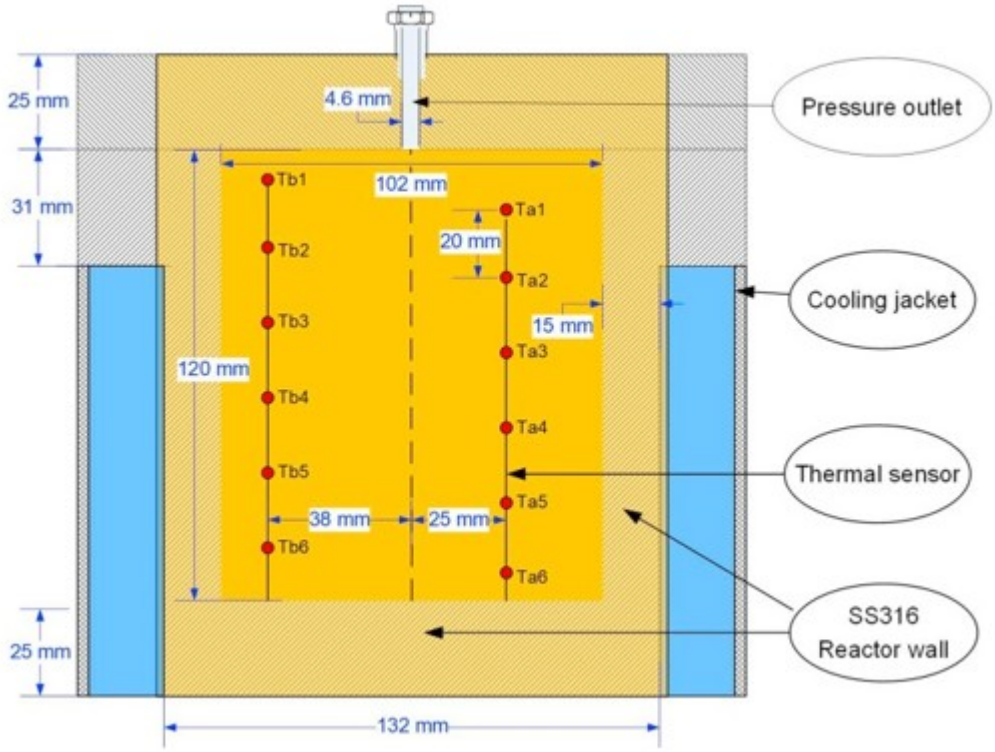

Fig. 2. Schematic of the cross section view of the reactor for MH formation and dissociation experiment.

2.2. Sample preparation and hydrate dissociation experiment

The methane hydrate formation experiment was described in detail and numerically analysed in the earlier paper of Yin et al. [55]. Following the MH formation phase in the Chong et al. [19] experiment, the synthesized MH-bearing sediment was subjected to dissociation induced by depressurization to a backpressure of $P = 4.0$ MPa. The timeline of activities during this dissociation phase of the experiment is shown in Fig. 3, and involves 3 steps in 2 different stages: Step S1 and S2 in the 1st (*preparatory*) stage, and Step S3 in the 2nd stage of hydrate dissociation and fluids production. The P and T data at key locations in the reactor were recorded at a frequency of 10.0 s. The P-T trajectory during the hydrate depressurization experiments with respect to the hydrate dissociation equilibrium curve are shown in Fig. 4. More specifically:

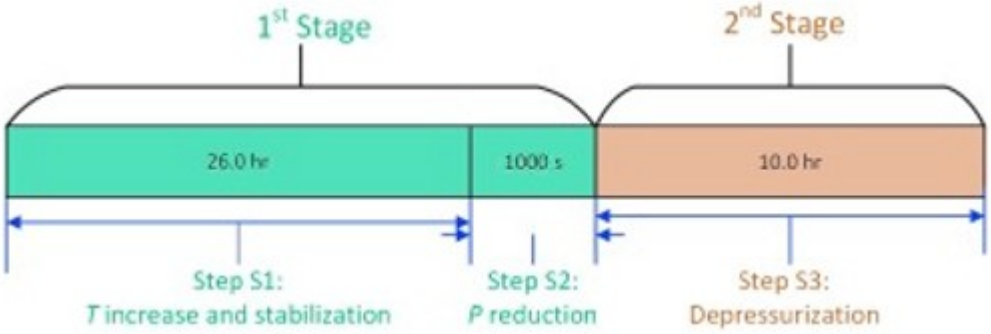

Fig. 3. Timeline of the depressurization-induced MH dissociation experiment (not to scale).

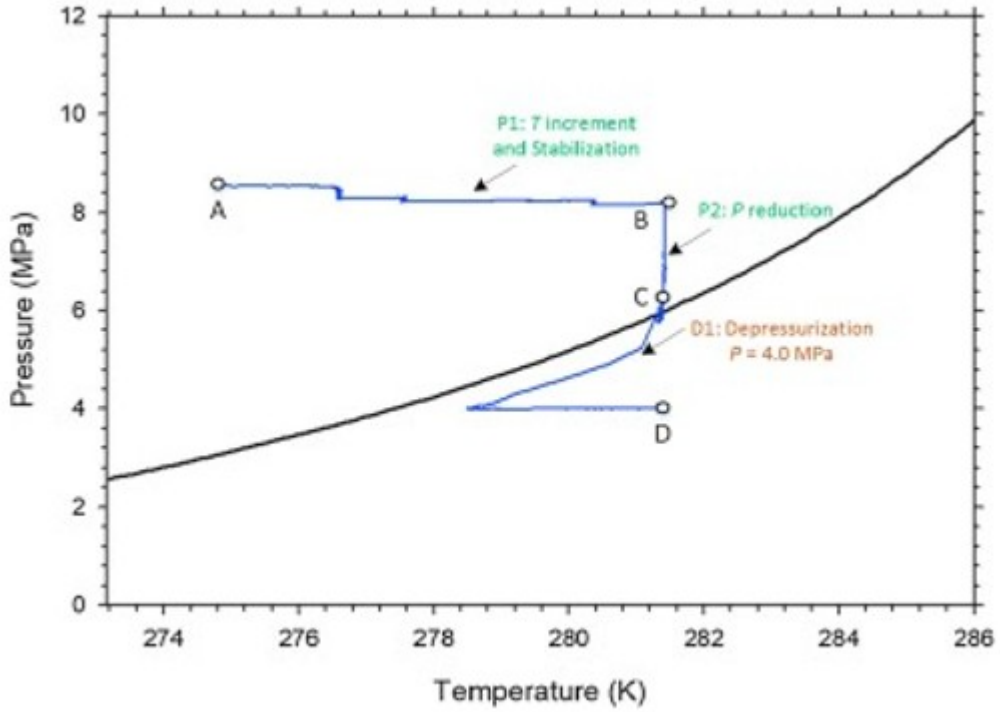

Fig. 4. *P-T* trajectory of the pressure-induced MH dissociation experiment analysed in this study with respect to the MH equilibrium curve.

1st Stage. Step S1 (A → B in Fig. 4: A 26.0 h-long step, during which the system temperature was increased from $T = 273.5\,\mathrm{K}$ to $T = 281.0\,K$ in the step-wise manner depicted in Fig. 5a through a circulating warm-water bath.

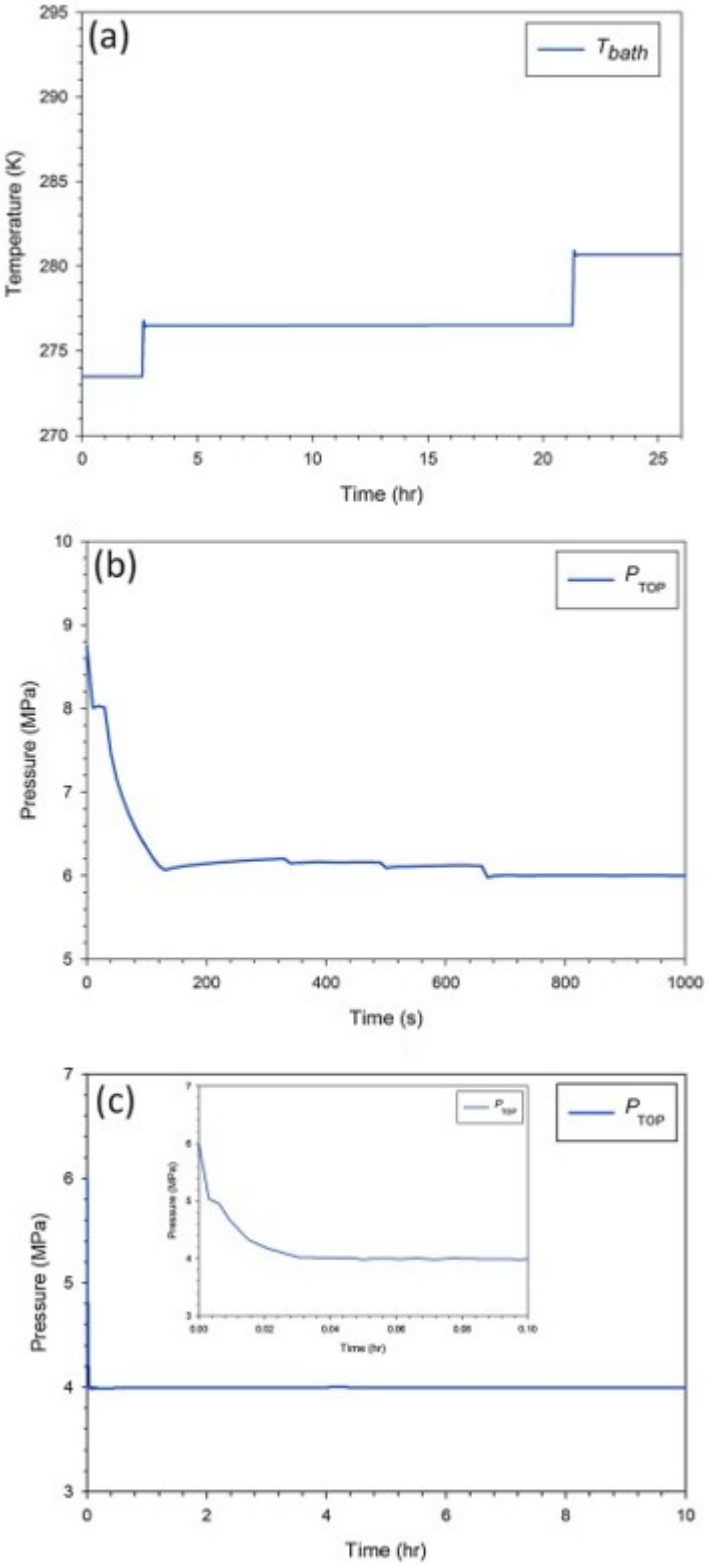

Fig. 5. Experimental measurement of (a) *T* of circulating water bath surrounding the reactor over time during Step S1, and of (b) *P* at the reactor pressure outlet during Step S2 and (c) Step S3.

1st Stage, Step S2 (B → C in Fig. 4: A 1000 s-long pressure reduction step (to a level above the equilibrium pressure), during which the system pressure was reduced from $P = 8.7$ MPa to 6.0 MPa through valve "V_4" (see Fig. 1 in the process depicted by Fig. 5b.

2nd Stage, Step S3 (C → D in Fig. 4: A 10 h-long step of hydrate dissociation and fluids production, during which the system pressure was reduced via the control valve "*CV*" (see Fig. 1 to the design backpressure of $P = 4.0$ MPa in the manner described by Fig. 5c.

The temperature increase during Step S1 was realized by adjusting the temperature of the circulating water bath (designated as "*RC*" in Fig. 1 as shown in Fig. 5a. This time-dependence variation in temperature is faithfully used as a boundary condition in our numerical study. The temperature of the water bath was kept constant during Steps S2 and S3. The *P*-reduction in Step S3 was achieved through a control valve (labelled "*CV*" in Fig. 1installed downstream of the reactor pressure outlet. The PID controller on the control valve effected the pressure reduction to the final design dissociation pressure of $P = 4.0$ MPa as shown in Fig. 5c. The evolution of pressure shown in Fig. 5c is used as a time-dependent boundary condition in the subsequent numerical analysis of the MH depressurization experiment.

These measurements of *P* and *T* will be used as the basis for the parameter-identification component of our numerical simulation study: the parameters that control dissociation are estimated by adjusting their values, leading to minimization of the deviations between observations and numerical results. In order to maintain consistency and continuity with the earlier study of Yin et al. [55], in the current study we did not attempt to further optimize the parameter values estimated (through history-matching) during the analysis of the MH-formation phase of the experiment. Thus, the properties determined from the Yin et al. [55]study were used unaltered, which significantly simplified the analysis and history-matching in the current study because it reduced the number of parameters-to-be determined to the following: (a) the surface area adjustment factor (F_A) in the hydrate dissociation kinetic reaction model [38], [56] (discussed in detail in Sections 3.4 The simulation approach and output of simulation results, 3.5 Hydrate dissociation kinetic models and surface area estimation), and (b) the parameters associated with the relative permeability and capillary pressure of the porous medium. Note that the latter were of limited importance during the formation phase of the experiments, but they are critically important during the dissociation and production phase covered by the present study.

3. The numerical model and the simulation approach

3.1. The T+H numerical model

The simulations in this study were conducted using the T + H code [57], [58], a numerical simulator developed at the Lawrence Berkeley National Laboratory (LBNL) to model the non-isothermal behaviour of CH_4 release,

phase change and flow under conditions typical of CH_4-hydrate deposits (i.e., in the permafrost and in deep ocean sediments, as well in any laboratory experimental set-up) by solving the coupled equations of fluids and heat balance associated with such systems. The simulator can model all the known processes involved in the system response of CH_4-hydrates in complex geologic media, including the flow of fluids and heat, the thermophysical properties of reservoir fluids, the thermodynamic changes and phase behaviour, and the non-isothermal chemical reaction of CH_4-hydrate formation and/or dissociation, which can be described by an equilibrium model [53] or a kinetic model [55]. T + H is a fully implicit compositional simulator, and its formulation accounts for heat and the various mass components that are partitioned among four possible phases: gas (G), aqueous (A), ice (I), and hydrate (H). The T + H code can describe all the 15 possible thermodynamic states (phase combinations) of the $CH_4 + H_2O$ system and any combination of the three main hydrate dissociation methods: depressurization, thermal stimulation and the effect of inhibitors. It can handle the phase changes, state transitions, strong nonlinearities and steep solution surfaces that are typical of hydrate formation and dissociation problems. A detailed description of the code, its underlying physics and capabilities, of the numerical techniques and of the various options it provides can be found in Moridis [57], [58].

3.2. Simulation domain and discretization

We used the MeshMaker v1.5 application [59] to construct the grid of the 2D axisymmetric cylindrical simulation domain (shown in Fig. 6) that represented accurately the geometry of the hydrate reactor, as described by Table 2 and Fig. 2. For maximum accuracy, and from the experience gleaned from previous simulation studies [60], [61], [62], [63], [64], [65], [66], we used a very fine spatial discretization. The interior of the reactor (with a radius $r = 51.0$ mm) was discretized into 26 (mostly uniformly-sized) subdivisions ($1 \times \Delta r = 1.0$ mm and $25 \times \Delta r = 2.0$ mm), and the reactor wall thickness ($d_{wall} = 15.0$ mm) was discretized into 5 uniformly-sized subdivisions ($5 \times \Delta r = 3.0$ mm) in order to accurately capture heat transport between the interior of the reactor and the circulating water. One additional outermost subdivision ($\Delta r = 0.1$ mm) was added to describe the time-dependent temperature boundary (see Fig. 5a) of the water bath (marked as red in Fig. 6. The internal height of the reactor ($d = 120.0$ mm) is discretized into 48 uniformly-sized subdivisions in z ($48 \times \Delta z = 2.5$ mm). In addition, the metal thickness of the top and bottom of the reactor vessel ($d_{top} = d_{bot} = 25.0$ mm) was discretized into 5 uniform subdivisions ($5 \times \Delta z = 5.0$ mm), with the outermost layer depicting the ambient (constant-temperature) air boundary (marked as yellow in Fig. 6. The two elements located at the top centre of the reactor (marked as green in Fig. 6represented the pressure outlet (with a radius $r_{outlet} = 2.3$ mm), to which the time-dependent pressure boundary condition (see Fig. 5b and c) was applied. In total, the cylindrical simulation domain was discretized into $32 \times 58 = 1856$ gridblocks in (r, z). The fine

discretization is important in the effort for accurate predictions in the small reactor system [19], as it is necessary to capture the hydrate dissociation fronts and the dynamic flow behaviour expected near the reactor outlet. With no inhibitors (such as salt) in the system, the domain discretization and the assumption of a kinetic hydrate dissociation reaction resulted in a total of 7424 simultaneous equations.

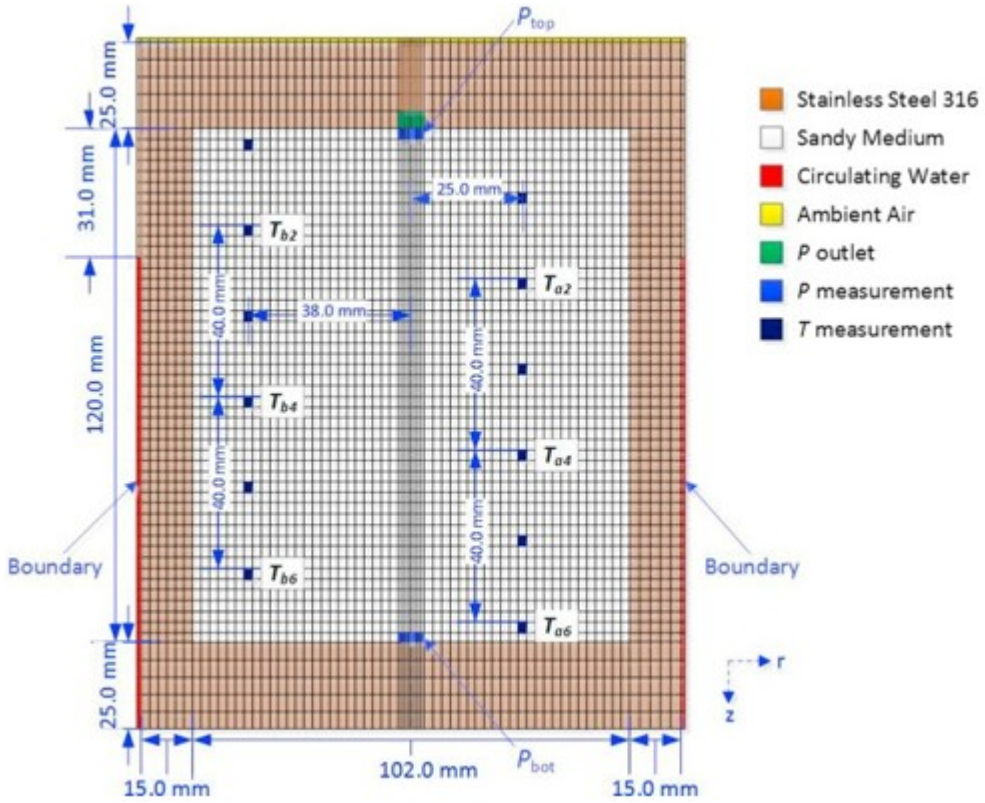

Fig. 6. Schematic of the mesh of the simulation domain accurately represents the reactor shown in Fig. 2.

3.3. System thermophysical properties, initial and boundary conditions

Table 3 summaries the key thermophysical properties of the fine quartz sand used in the experiment, of the metal parts of the reactor, and the parameters for the constitutive models involved in the simulator. Note that some of the listed properties of the sandy porous medium were obtained from direct measurements from laboratory tests and are marked by a star (‘*’) superscript; others were derived from the parameter identification (history-matching) process in the earlier numerical study on MH formation of Yin et al. [55] and MH dissociation in this study, and are marked by a “−” and a “+” superscript respectively. The composite thermal conductivity model in this study follows the linear composite model described in [57], which accounts for all three phases. In the absence of direct measurements, the parameter values of Table 3 that are associated with the relative permeability [67] and the capillary pressure models [68], [69] were representative of sandy materials. The kinetic equation of hydrate formation

follows the Kim-Bishnoi [38] and the Clarke and Bishnoi models [56] (see Section 3.5). In Table 3, the values of the surface area adjustment factor F_A power function that is of paramount interest to the present study represents the final estimate and is evaluated through a history-matching process that minimizing deviations between the experimental data and the numerical predictions. In addition, Table 4 summarizes the boundary conditions for each step and the initial condition before Step S3, which is the critical step for hydrate dissociation and fluids production.

Table 3. Thermophysical properties of materials and parameters of constitutive models.

Parameter	**Value**
Gas composition*	100% CH_4
Hydration number $(N_H)^{-}$	6.0
Absolute permeability $(k)^{*}$	$k_r = k_z = 3.83 \times 10^{-12}\,\mathrm{m}^2$
Porosity of sandy medium $(\phi)^{-}$	0.448
Absolute permeability of pressure outlet^{+}	$k_r = 0\ k_z = 5 \times 10^{-9}\,\mathrm{m}^2$
Porosity of pressure outlet^{+}	1.0
Density of quartz sand $(\rho_s)^{*}$	2650 kg/m^3
Density of SS316 (ρ_{ss})	8000 kg/m^3
Thermal conductivity of sand under dry condition $(k_{\theta d})^{+}$	1.20 W/m/K
Specific heat of quartz sand $(C_R)^{-}$	1309 J/kg/K
Thermal conductivity of SS316 $(k_{\theta S})$	16.0 W/m/K
Specific heat of SS316 (C_S)	500 J/kg/K
Thermal conductivity of water (k_{water})	0.60 W/m/K
Thermal conductivity of air (k_{air})	0.024 W/m/K
Composite thermal conductivity model $(k_\theta)^{+}$[57]	kθ=kθd+ϕ(kθASA+kθHSH+kθGSG)
Relative permeability model (Stone's model [67])$^{+}$	krA=SA-SirA1-SirAnA
	krG=SG-SirG1-SirGnG
n_A	5.0
n_G	3.5
S_{irA}	0.05

Parameter	Value
S_{irG}	0.01
Capillary pressure model (vG model [68])+	Pcap=-P0[(S∗)-1/λ-1]1-λ
	S∗=SA-SirASmxA-SirA
S_{irA}	0.049
λ	0.50
P_0 (Pa)	5×10^3
S_{mxA}	1.00
Hydrate dissociation kinetic rate model (Kim et al. [38])+	nH=FAK0ASexp-ΔERT(feq-fg)
Hydration reaction constant (K_0)	3.6×10^4 mol/m^2 Pa s
Activation energy (ΔE)	81.0 kJ/mol
Reaction surface area (A_S)	Eq. (2), (3)
Surface area adjustment factor (F_A) +	Table 5

Table 4. Boundary conditions for Step S1, S2 and S3 with initial condition for Step S3.

Boundary condition	Value
Step S1	Change of T (see Fig. 4a)
Step S2	Change of P (see Fig. 4b)
Step S3	Change of P (see Fig. 4c)
T_{air} (K)	295.2
Initial condition (Step S3)	**Average value (see Fig. 11 for spatial distribution)**
P	6.0 MPa (see Fig. 11a)
T	281.0 K (see Fig. 11b)
S_H	40.27% (see Fig. 11c)
S_A	57.67% (see Fig. 11d)
S_G	2.06% (see Fig. 11e)

3.4. The simulation approach and output of simulation results

The modelling process duplicated numerically all the steps in the two stages described in Section 2.2, and was designed to address the objectives discussed earlier. As discussed earlier, the analysis of the MH formation in the sister study of Yin et al. [55] has already led to the estimation of several properties (i.e., of ϕ, S_{irA}, $C_{R,}$ $k_{\theta w}$, F_A and N_H) through the history matching method of Thomas et al. [70]. Some of these properties (ϕ, S_{irA}, $C_{R,}$ $k_{\theta w}$, and N_H) are relatively well quantified and are unaffected by the change from hydrate formation to dissociation. Thus, the focus of this study (as guided by scoping simulations involving sensitivity analysis) were the determination of (a) the surface area adjustment factor (F_A) which essentially controls the kinetic rate of hydrate dissociation and fluids production, and (b) the parameters in the relative permeability and the capillary pressure models, with some minor adjustments of the thermal properties.

During Step S1 in the 1st (preparatory) stage, a time-dependent temperature (see Fig. 5a) was applied to the boundary representing the circulating water location (see Fig. 6. During Step S2 and S3, a time-dependent pressure boundary was applied (see Fig. 5b and c) to the appropriate location (i.e., the pressure outlet) at the top of the reactor. Because of the difficulties, imperfections and inaccuracies associated with the monitoring/measurement of temperatures, the data sets to be used in the optimization (history-matching) process in terms of decreasing importance are: the cumulative gas production volume (V_G), the cumulative water production mass (V_A), the pressure at key locations, and (last) the temperature (T) measurements at the points identified in Fig. 6.

The experiments of Chong et al. [19] monitored the system pressure response at the top and bottom centre (P_{top} and P_{bot}), the temperature response at the 6 different thermocouple locations (T_{a2}, T_{a4}, T_{a6}, T_{b2}, T_{b4}, T_{b6}) shown in Fig. 6. In our study, we monitor the numerical predictions of P and T at the same locations over time. Additionally, we monitor the spatial distributions of important variables (P, T, S_A, S_H, S_G) at different times during each one of Steps S1, S2 and S3. The system behaviour is monitored frequently during the first 5 min of Step S3 in order to capture its early dynamic response (caused by the fast pressure reduction at the beginning of this step).

3.5. Hydrate dissociation kinetic models and surface area estimation

In our earlier study [53], we highlighted the importance of kinetic retardation in the time-scales associated with laboratory experiments. In addition, it should be noted from the study of Kowalsky and Moridis [71] that the implementation of kinetic reaction model of hydrate dissociation is necessary in short-term (minutes to hours) and core-scale (centimetre to meter) simulations, whereas the equilibrium reaction model can be a viable alternative to the kinetic model for large-scale (tens of meters to kilometres) and long-term (days to years) production simulations with minor differences.

The T + H code uses the kinetic model of Kim et al. [38] and Clark and Bishnoi [56], which is described by the following equation:

(1)nH=FAK0ASexp-ΔERT(feq-fg)

In Eq. (1), the values of K_0 and ΔE were kept constant at the level specified by Clark and Bishnoi (see Table 3. One complication in the kinetic rate model is the estimation of the hydrate surface area (A_S) in geologic media, which dependents significantly on the geometry and location of the hydrate particles in the pore space. Based on an assumption of spherical hydrate particles distributed in the void space between spherical media grains shown in Fig. 7, and using the Kozeny-Carman equation, Moridis [57], provided an estimate of A_S as

(2)AS=0.8791-ϕrpSH2/3

where ϕ is the medium porosity, and r_p is the average grain radius estimated from

(3)rp=45k(1-ϕ)2ϕ31/2

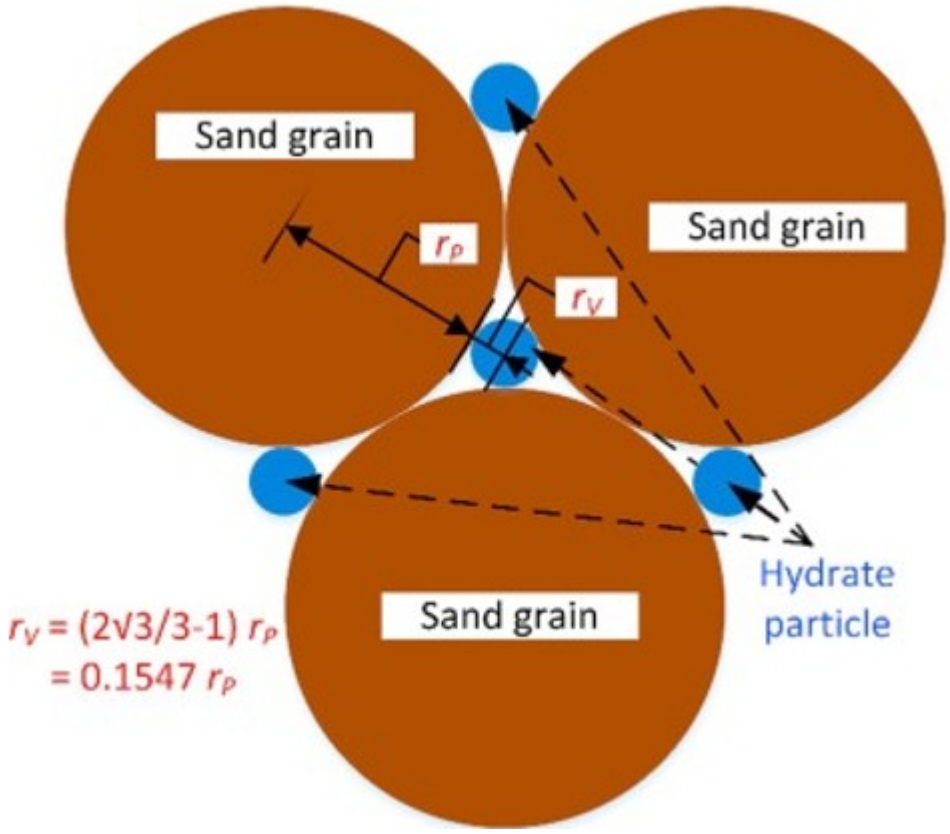

Fig. 7. Schematic of spherical hydrate particles in the pore space of spherical sand grain [57].

An important issue in Eq. (1) is the surface area adjustment factor (F_A), which quantifies the area over which the hydrate reaction occurs. F_A in essence is an adjustment to the combined product of the kinetic reaction constant K_0 of the hydrate reaction and of the area of the reaction surface A_S, and also

accounts for deviations of the reaction surface area from the initial assumption of sphericity. For the current study, after scoping calculations pointing in this direction, the T + H v1.5 simulator [57] was modified to describe F_A as a power function of time (instead of a constant), and the parameters of the function were determined through the history-matching process.

4. Simulation results and discussion

4.1. Step S1

Fig. 8 shows the evolution of P and T at the key locations (see Fig. 6) described in Section 3.4, as well as the changes in the mass of the various phases (A, G and H) over time during Step S1. Fig. 8a shows a good match between the simulated and experimentally-measured P, which increased slightly from the initial level of $P = 8.7$ MPa at $t = 3.0$ h and at $t = 22.0$ h, when the T of the circulating water was raised stepwise from $T = 273.5$ to $T = 276.5$ K and $T = 281.0$, respectively. This can be attributed to the thermal expansion of the hydrate bearing sediment, as well as to the gas exsolution from the aqueous phase. This is evidenced by the increase in the free gas mass shown in Fig. 8b.

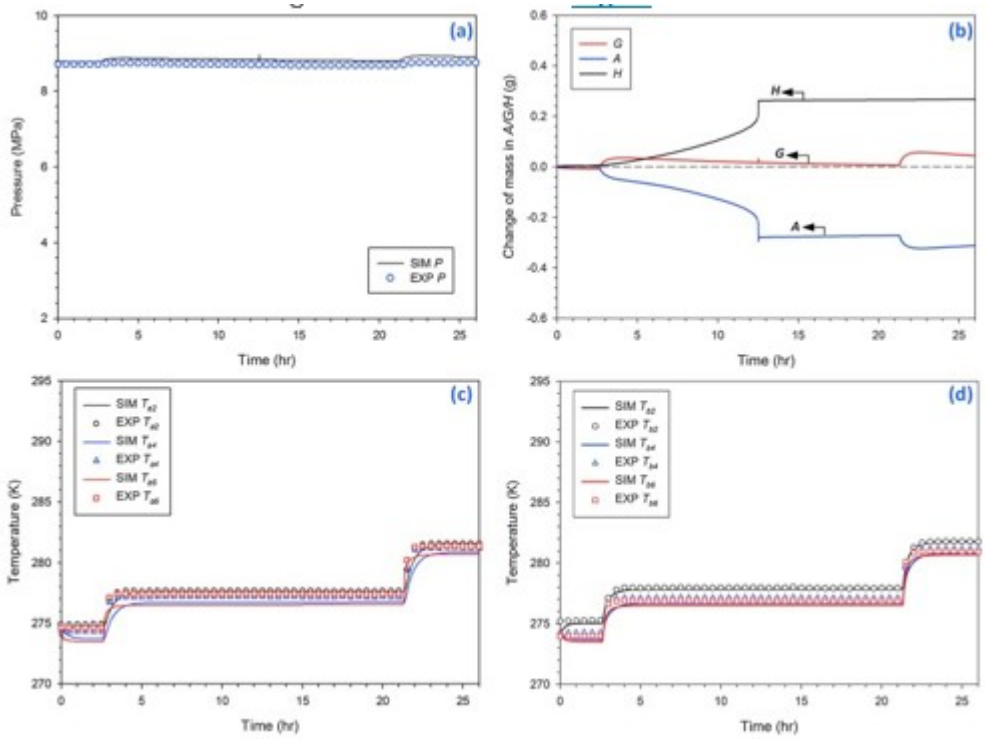

Fig. 8. Evolution of P, T, and of the mass change in the mass of the various phases (A, G and H) in the reactor over time during Step S1.

Fig. 8b shows the changes in the mass of the various phases during Step S1. The mass of free gas increases after each T- increase, as the solubility of gas in H_2O decreases. The mass of hydrate increases at a slow rate as the temperature increases, as gas released from solution combines with H_2O to

form hydrate. This is also shown by the corresponding decrease in the mass of free H_2O and gas over time. The hydrate mass continues to increase but at much lower (almost imperceptible) rate for $t > 12.5$ h because of the exhaustion of the free CH_4 gas. This is reflected by the very slow decline of free CH_4 in the system, which continues until the 2nd increase in temperature at $t = 22.0$ h. More gas is released in a "burst" at that time, and that release is followed by a very slow decrease caused by a correspondingly slow hydrate formation. Note that for $t > 22.0$ h, the loss in the mass of the aqueous phase reflects faithfully the release of dissolved CH_4 in water. The raised temperature and the kinetic retardation (optimized $F_A = 10^{-6}$, see Table 5) limit significantly additional hydrate formation in the remainder of Step S1.

Table 5. Optimized value of the surface area adjust factor (F_A) in Step S1, S2 and S3.

Step	Value
S1	$F_A = 10^{-6}$
S2	$F_A = 10^{-6}$
S3	$F_A = 1.32 \times t^{-0.72}$

Fig. 8c and d shows that the numerical results capture (a) the trends accurately and (b) the increase in T of the MH-bearing sediment in a satisfactory manner at different thermocouple positions. Note that matching numerically sensed temperatures is inherently difficult because of the effect of localized heterogeneities, of the sensor contact with materials of different properties (grains vs. the various phases), of possible imperfections in the underlying composite thermal conductivity model in the numerical simulator, and also because of the disequilibrium between the temperature of fluids and that of the grains – our simulation approach assumes thermal equilibrium.

It should be noted that with the consideration of the ambient temperature as a boundary above the top of the reactor leads to variations of T along the vertical z direction at the locations of the thermocouples. A higher T is observed at T_{a2} and T_{b2}, i.e., at positions closer to the top of the reactor. The T of the other thermocouples is more affected by their location relative to the circulating water. The difference in T between locations T_{b2} and T_{b6} is about 1.3 K, matching the experimental observation well.

Fig. 9 shows the evolution of the spatial distributions of P, T, S_H, S_A, and S_G over time during Step S1. Fig. 9a indicates that P is practically uniform in the reactor, which was expected given the large permeability $k = 3.8$ Darcy of the sandy medium, and the small volume of the reactor ($V = 0.98$ L). Fig. 9b is characterized by an expanding warm region at the top of the reactor because of its proximity to the top boundary (ambient air of a constant higher T), while the T of the vertical walls and of the bottom of the reactor is

close to (and controlled by) the temperature of the circulating water ($T = 281.0$ K) at these locations. Fig. 9b clearly demonstrates that the thermal effect of a boundary of ambient air on the reactor system should not be underestimated. The S_H distribution during the entire Step S1 in Fig. 9c shows limited deviation from that at the end of the hydrate formation, which is characterized by significant spatial heterogeneity: $S_H = 65\%$ near the reactor bottom, and $S_H = 5$–10% toward the outlet and centre of the reactor. The only S_H change in Step S1 is the formation of minuscule amounts of additional MH near the top of the reactor. Similar to the S_H distribution in Fig. 9c, the S_A distribution in Fig. 9d remains practically unchanged during Step S1, the only difference being the imperceptible S_A reduction that mirrors the corresponding hydrate formation in Fig. 9c. The change of S_G in Fig. 9e, though, is significant (in relative, if not in absolute, terms) and reflects the gas release evidenced in Fig. 8b and discussed earlier. Note the gas-free region near the top of the reactor, which is evident in all 3 panels of Fig. 9e. This is caused by the last H_2O injection during the hydrate formation process (see Yin et al. [55], and persists during the 26 h of Step S1 because of capillarity and the relative permeability regime (as controlled by the very limited amount of gas in the reactor) prevent redistribution of the gas phase.

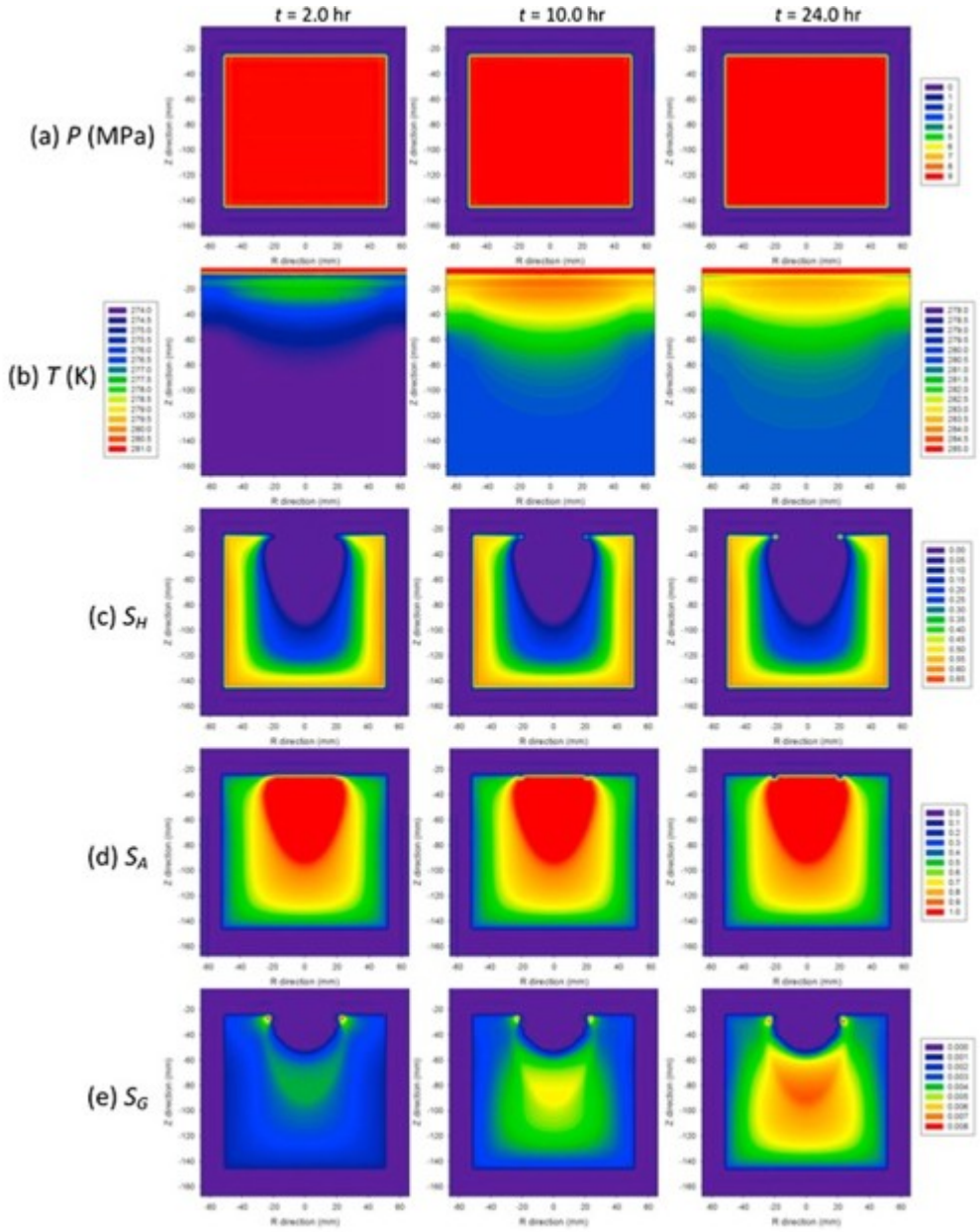

Fig. 9. Evolution of the spatial distributions of P, T, S_H, S_A, and S_G over time during Step S1. (Left T scale for $t = 2.0$ h and $t = 10.0$ h).

4.2. Step S2

Fig. 10 shows the evolution of P, T, and the change in the mass change of the three phases (A, G, H) in the reactor over time during Step S2. During the short duration of Step S2 (1000 s), there is a very good agreement of the numerical predictions and of the laboratory measurement of P (Fig. 10a). The match between prediction and observation of the evolution of T at all 6 monitoring positions (Fig. 10c and d) ranges between excellent and acceptable, but in general it is less satisfactory than that for P for the reasons already discussed in the previous section. The phase mass changes in Fig. 10b conforms to expectations: the pressure in the reactor is lowered,

but remains comfortably higher than the hydration equilibrium P at the reactor range of temperatures. Consequently, there is no change in the mass of hydrate. The mass of gas phase in the reactor increases by 0.25 g because of CH_4 exsolution from the aqueous phase, in addition to the larger contribution of H_2O vapour to the gas phase at the lower pressure. Based on the comparison of the simulation results, the mass of aqueous phase decreased by 19.0 g during the depressurization stage, mainly because of water removal from the reactor when the pressure was lowered (we regret being unable to capture and measure the fluids released through the V_4 valve (see Fig. 1, which would have provided an additional data point for the evaluation of the simulation approach). At the end of Step S2, the mass of the aqueous, gas and MH phases are 162.0 g, 0.4 g and 254.0 g, respectively. This translates into the following bulk saturations: $S_H = 40.27\%$, $S_G = 2.06\%$, and $S_A = 57.67\%$, respectively.

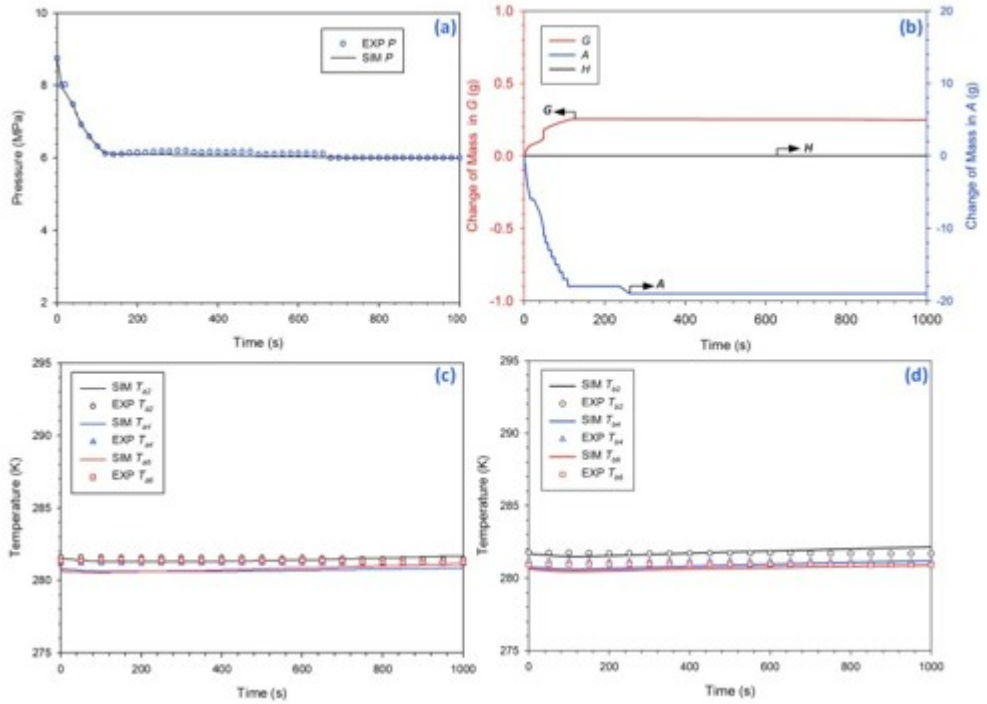

Fig. 10. Evolution of P, T, and of the change in the mass of the mass change of various phases (A, G and H) in the reactor over time during Step S2.

Fig. 11 shows the spatial distributions of P, T, S_H, S_A, and S_G at the end of Step S2. As expected, pressure was practically uniform throughout the reactor because of the reasons already explained. T is higher near the top of the reactor because of the warmer (ambient air) boundary with a low-T region in the reactor centre and bottom. For the reasons already explained in the discussion of Fig. 9b, the S_H distribution at the end of Step S2 (Fig. 11c) remains the same as at the end of Step S1 (Fig. 9c). Although the mass balance analysis in Fig. 10b indicates a mass loss of 19.0 g of the aqueous phase, this is not readily evident from the spatial distribution of S_A in Fig.

11d, which remains similar to that at the end of Step S1 (Fig. 9d) possibly because of the limited amount of water loss compared to the water mass in the system at that time. Obviously, most of the aqueous phase removed during Step S2 originated from the upper and centre parts of the reactor, where $S_A = 1$. The $S_G$distribution shown in Fig. 11e now occupies a region that was previously gas-free due to the depressurization from the pressure outlet, and occurs in the reactor at levels that are much higher than those observed at the end of Step S1. The reason for the higher S_G saturations is the exsolution of CH_4 from the aqueous phase as pressure in the reactor was lowered, and reflects the change in the gas phase mass shown in Fig. 10b.

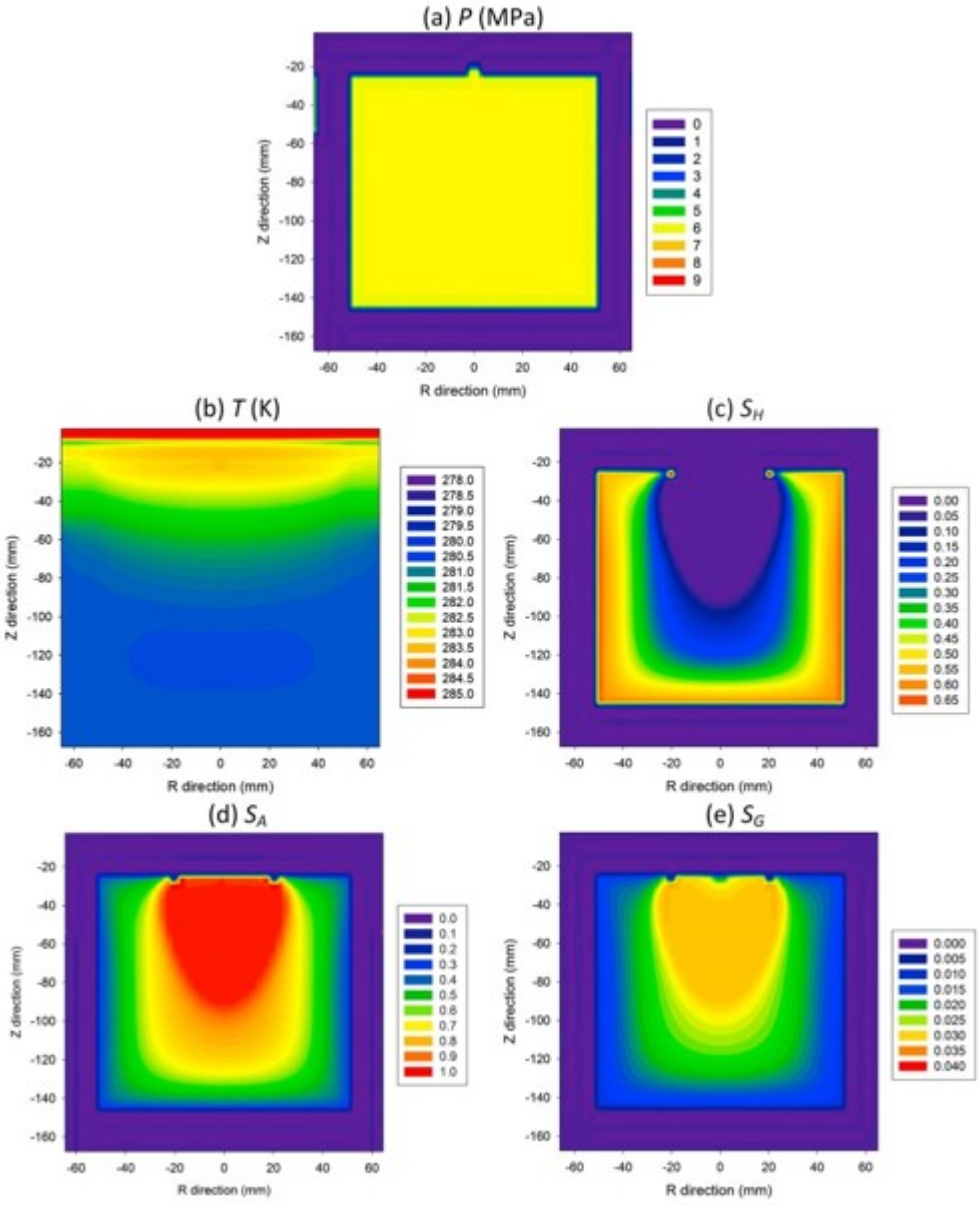

Fig. 11. Spatial distributions of P, T, S_H, S_A, and S_G at the end of Step S2.

4.3. Step S3

Fig. 12 presents the evolution of P, T, the cumulative gas production volume (V_G), the cumulative water production mass (V_A) and the mass of various phases in reactor (A, G, H) over time covering the entire duration of the depressurization during Step S3. There is an excellent agreement between the simulated and the predicted P at the monitoring locations (Fig. 12a) as pressure dropped according to the regime depicted in Fig. 5c from $P = 6.0$ MPa to 4.0 MPa during the first 2.0 min, and maintained almost constant at $P = 4.0$ MPa for the remainder of Step S3. Because of the continuous opening and closing of the control vale to control the pressure at the 4.0 MPa threshold, slight variations were observed during the experimental process, and these were fully implemented in the boundary conditions of the current simulation. Note that these numerical results, as well as all subsequent simulation results discussed in this section, were obtained using the optimized parameters listed in Table 3 that were determined through the history-matching process (involving minimization of deviations between observations and simulation results).

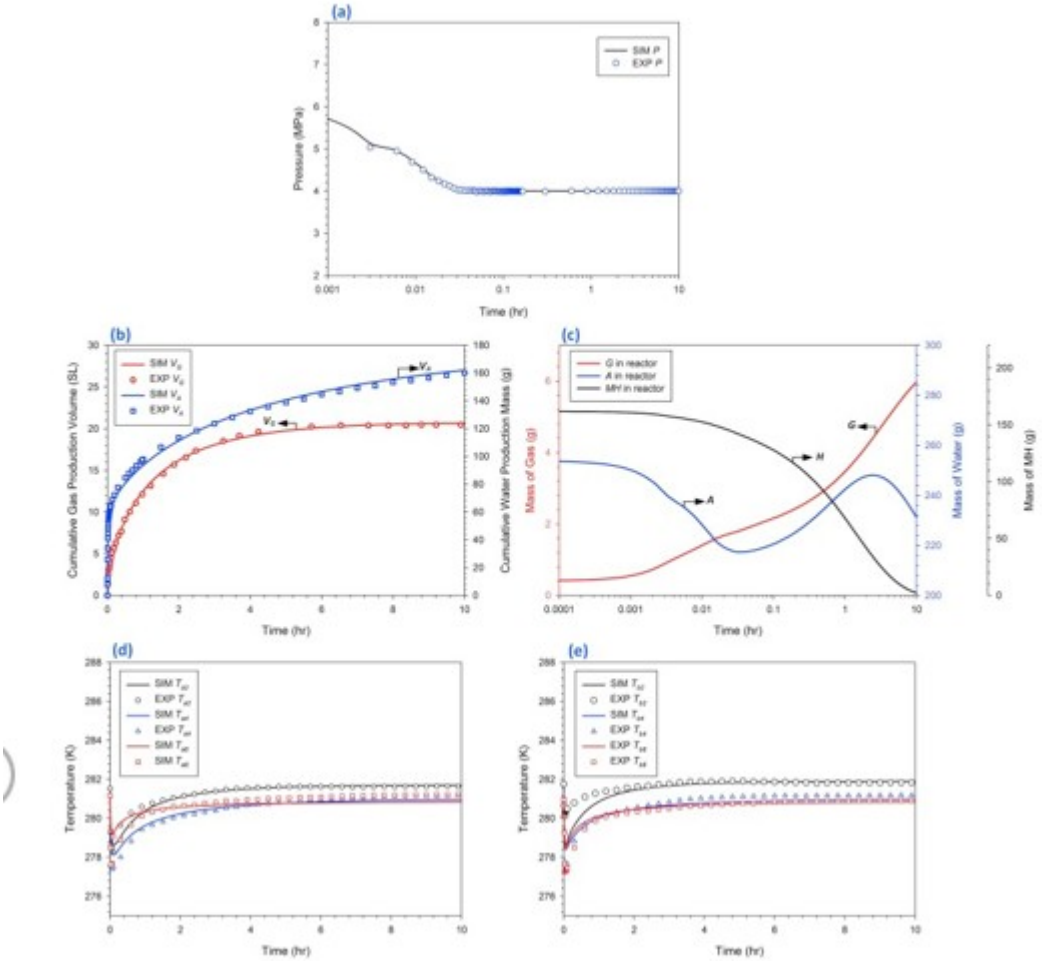

Fig. 12. Evolution of P, T, of the cumulative gas production volume (V_G), of the cumulative water production mass (V_A), and of the mass of various phases (A, G, H) in the reactor over time during Step S3.

Using the optimized parameters determined from this study (as well as the optimized parameters determined from the earlier study of Yin et al. [55], we estimated numerically the produced gas volume V_G and water mass V_A shown in Fig. 11b, which are in excellent agreement with the experimental results obtained during the experiment. More specifically: the final volume of V_G predicted from the simulation is 20.2 SL and the measured volume of produced gas (Chong et al., [19]was 20.1 SL. This corresponds to an overall CH_4 recovery ratio of 67.8% (with the rest of the gas either remaining in the reactor or having been removed earlier during the pressure-lowering Step S2). Fig. 11c shows the evolution of the masses of the various phases in the reactor: the mass of the aqueous and gas phases ($M_A$and M_G, respectively), as well as the mass M_H of the dissociating hydrate as it declines toward zero (= complete dissociation). The evolution of M_G shows monotonically increase in the reactor as gas releases from hydrate dissociation, and the evolution of M_A shows variations, which are caused by the pattern (initial fast) of water removal from the reactor through the pressure outlet and the hydrate dissociation.

Comparison of the estimated and measured T at the various monitoring locations (Fig. 11d and e) shows a good agreement and indicates that the simulation clearly captures the pattern and trend (as well as the magnitude) of the T-evolution, including the sharp initial decline caused by the endothermic hydrate dissociation. The (early) deviations that are observed are attributed to dynamic nature of T-change during the most active phase of dissociation (i.e., when the pressure is suddenly lowered to the 4.0 MPa level), as well as to the difficulties and challenges associated with T-studies that were discussed earlier in Section 4.1. For example, the faster initial warming seen in the experimental observations at the T_{b2} location is attributed to significant heterogeneity and the very dynamic nature of early dissociation at that location (next to the depressurization point): hydrate does exist there (as evidenced by the initial sharp T-drop), but the faster T-recovery suggests lower $S_H$saturation and the warmer T-boundary at reactor top. Such deviations decline significantly at the monitoring locations closer to the bottom of the rector, where MH occurs at higher saturations and which responds later (than the top) to the dissociation stimulus.

The spatial distribution of key variables (P, T, S_H, S_A, and S_G) during Step S3 are presented in Fig. 13, which describes the system response at $t = 0.5$, 5.0 min, 1.0 h, 5.0 h and 7.0 h. During the first 5.0 min of Step S3, P decreases from $P = 6.0$ MPa to $P = 4.0$ MPa, and the P-distribution at any time during this interval is practically uniform in the entire reactor (Fig. 13a) for reasons already discussed. The continuous decline in temperature over time in Fig. 13b is the result of the endothermic nature of the MH dissociation (which is fuelled by the sensible heat of the system). Compared to the T-distribution at the end of Step S2, a low-Tregion evolves from $t = 0.5$ min to $t = 5.0$ min as the cold fluids move from their release points (along the walls and bottom of the reactor where MH is concentrated, see Fig. 10c) toward

the pressure outlet. The *T*-distribution in Fig. 13b shows an interesting development: while the continuing dissociation at the constant *P* in the reactor results in the cooling determined by the equilibrium temperature, the volume of the low-*T* region keeps shrinking (and the average temperature keeps increasing) for $t > 5.0$ min because of the heat inflow from the water bath (along the walls and the bottom of the reactor) that is now warmer than the hydrate. In other words, depressurization (caused by the lower pressure at the "*CV*" valve) is accompanied by heat inflows from the boundaries (the warmer water bath and ambient air in this case). The result of the warm temperature boundary is the significant increase in the temperature, which is expected to enhance MH dissociation.

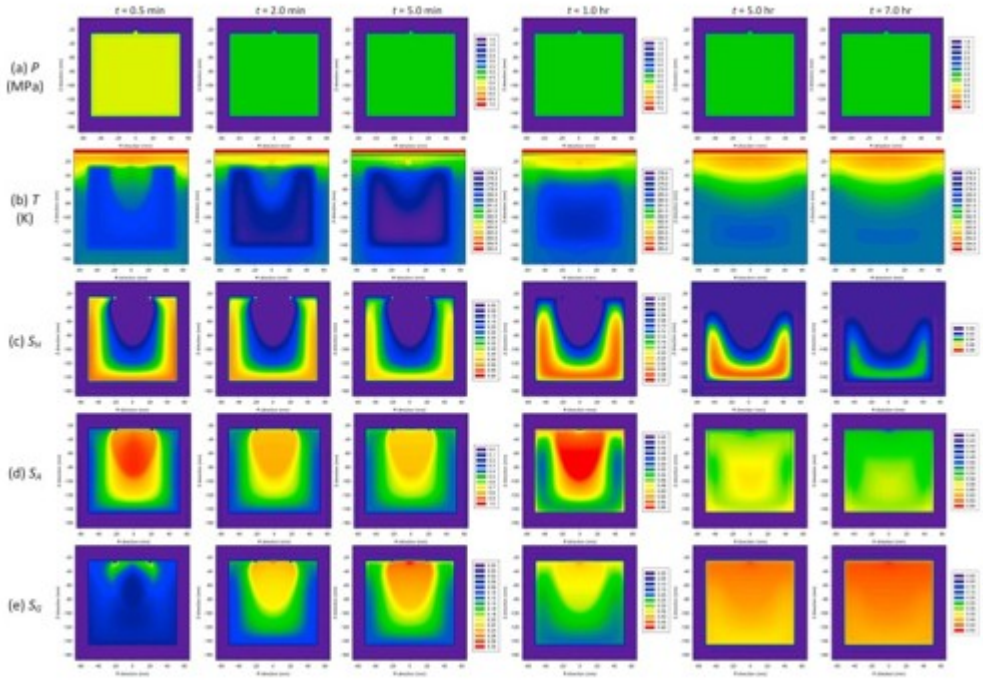

Fig. 13. Spatial distribution of *P*, *T*, S_H, S_A, and S_G over time during Step S3 at $t = 0.5$ min, 2.0 min, 5.0 min, 1.0hr, 5.0 h and 7.0 h (all scales are to the right of the figure).

Because of continuing MH dissociation (Fig. 12c), Fig. 13c shows a continuous reduction in both the MH volume (footprint) and the magnitude of S_H as time advances. The $S_H$distribution confirms the earlier deduction (based on the *T*-distribution) that dissociation occurs in the entire MH mass (indicated by the lowering of S_H throughout the MH mass), with the footprint of the hydrate-free portion of the reactor volume expanding from the interior toward the boundaries.

Because of the continuous production of fluids during Step S3, S_A in Fig. 13d declines with time (compared to the maximum level observed in the reactor at the end of Step S2, see Fig. 11d). On the other hand, the footprint of the reactor volume where $S_A > 0$ appears to expand, as MH dissociation leads to H_2O release near the reactor boundaries. The S_G distribution in Fig. 13e shows the initial response of fast gas production (see Fig. 12b) at $t = 0.5$ min

where a low S_G region developed earlier near the pressure outlet. The low S_G region reinstates back quickly to its original pattern (at the end of Step S2, see Fig. 11e) at $t = 5.0$ min, but to a much higher level due to the gas releases from MH dissociation and to a much lower extent, from exsolution from the aqueous phase from the depressurization.

This is confirmed by the S_H distribution in Fig. 13c, which shows MH destruction from the top (controlled by the depressurization through the pressure outlet) and from its outer perimeter (vertical and bottom boundaries, controlled by the heat inflow from the boundary). Fig. 13c shows that the total MH mass continues to decline during Step S3, as expected because of the continuing dissociation stimuli and confirmed by the MH estimate in Fig. 12c. At $t = 5.0$ h, there is still a fair amount of hydrate in the reactor, but the continuing dissociation has reduced with maximum S_H to the 10% level. Fig. 13d and e show that the distributions of $S_A$and S_G become more uniform over time and attain higher levels, as the aqueous and gas phases occupy an expanding volume of the reactor previously occupied by the dissociating MH hydrate. The highest S_A and S_G levels are observed in the upper central part of the reactor, through which the reactor fluids flow on their way to the pressure outlet and withdrawal from the system.

Of particular interest is the evolution of the surface adjustment factor (F_A) during Step S3, as determined from the history-matching process. The optimized power function of $F_A = F_A(t)$ is plotted in Fig. 14. The large value of $F_A = 100$ during the first 10^{-4} hr suggests that during the initial stage of depressurization (when pressure is abruptly lowered to 4.0 MPa), hydrate dissociation practically approaches an equilibrium reaction, and hydrate dissociation is strongly limited by the heat transfer from its surrounding. Following its very high initial value, F_A decreases continuously during the remainder of dissociation to a final level on the order of 10^{-2}, which indicates that kinetic retardation is significant during this stage. The rapid decline in the value of F_A with time reflects the decline in the driving force and the possible shrinking of the hydrate particle surface area against time during the depressurization experiment of Chong et al. [19]. Compared to the value of F_A calibrated from the earlier analysis of MH formation experiment (on the order of 10^{1}–10^{-6}, see Yin et al. [55], it appears that the kinetic retardation effect is less significant in the MH dissociation process than in the MH formation process. This finding can also be corroborated by the molecular measurement of methane hydrate dissociation kinetics using nuclear magnetic resonance (NMR) spectroscopy by Gupta et al. [72]: the unit cell of sI methane hydrate was dissociated as a whole with no preferential decomposition of large and small cages; whereas, in methane hydrate formation, formation of large cages ($5^{12}6^{2}$) is slower than that of small cages (5^{12}) [73]. Such kinetic behaviour was also suggested by the numerical study of Sun and Mohanty [47], which indicated orders of difference between the kinetic rate constant for hydrate formation and dissociation.

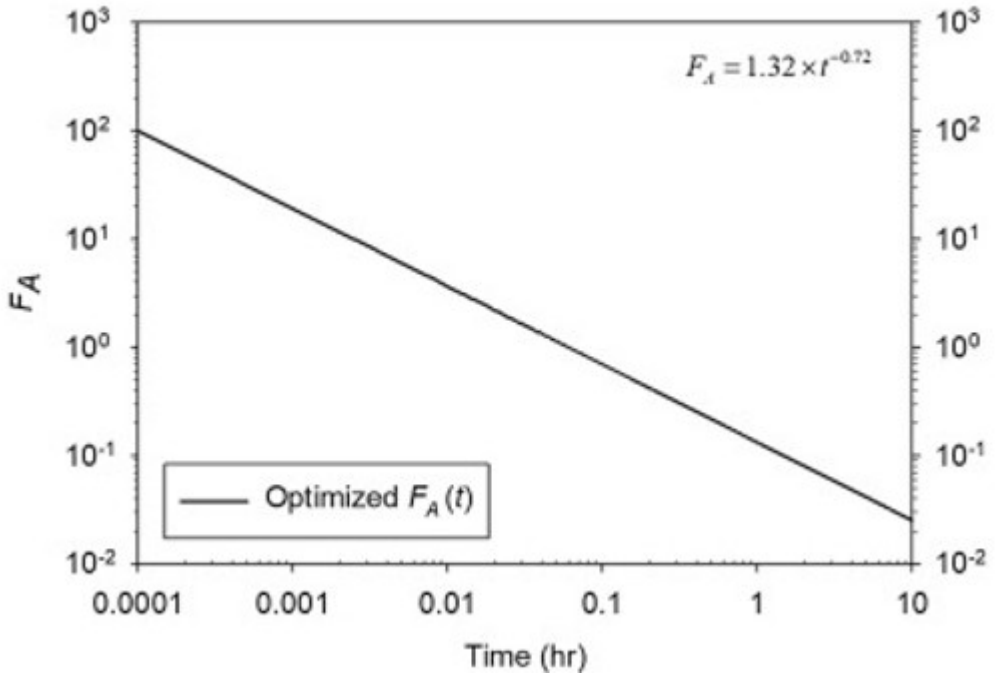

Fig. 14. Optimized surface area adjustment factor (F_A) in Step S3.

5. Summary and conclusions

We analysed by means of numerical simulation the laboratory experiments of depressurization-induced MH dissociation [19], for the first time using as initial conditions the spatially-heterogeneous distribution of the phases present in the system (aqueous, gas and hydrates) estimated from the earlier study of Yin et al. [55]. The study was conducted using the T + H v1.5 code of Moridis [57] and invoked the option of a kinetic dissociation reaction that followed the model of Kim et al. [38] and Clarke and Bishnoi [56]. The numerical simulation faithfully reproduced the geometry of the laboratory apparatus, the heterogeneous initial and boundary conditions of the system and the parameters of the dissociation stimulus, capturing accurately the 3 steps of the experimental process: (a) a preparatory, 26-h-long Step S1, during which the temperature was raised from $T = 273.5$ K to $T = 281.0$ K through a circulating warm-water bath; (b) a short (1000 s) preparatory Step S2 involving a pressure reduction from $P = 8.7$ MPa to 6.0 MPa (above the equilibrium dissociation pressure at 281.0 K); and (c) a longer (10 h) Step S3 of hydrate dissociation and fluid production, during which the system pressure was reduced to the design backpressure of $P = 4.0$ MPa.

Using inverse modelling (history-matching) that minimized deviations between the experimental observations and numerical predictions, we determined the values of all the important flow, thermal and kinetic parameters that control the system behaviour, which yielded simulation results that were in excellent agreement with the measurements of key monitored variables, i.e. the pressure, temperature, cumulative production of gas and water over time.

The following conclusions are drawn from this study:

1. In Step 1 of the preparatory Stage 1, the rising T leads to a slightly higher pressure P, both of which are safely within the hydrate stability zone. The P and T shifts cause a slight change in the relative mass of the phases in the system. Thus, there is a slight reduction in the mass of the aqueous phase that mirrors an equivalent increase in the mass of the hydrate, and reflects the decrease in CH_4-solubility in H_2O at Tincreases. This, coupled with the resulting higher P because of phase expansion caused by the higher T, leads to exsolution of CH_4 from the aqueous phase and to additional hydrate formation.

2. The pressure decline in Step 2 of the preparatory Stage 1 does not affect the mass of the hydrate phase because it is still within the hydrate stability zone.

3. In Steps 1 and 2, the overall changes are mild and can be adequately described by the kinetic model of the hydrate formation/dissociation reaction using values of the surface area adjustment factor F_A that (a) are different for each step, but (b) remain constant for the duration of each step.

4. During the MH dissociation in Step 3, the changes are rapid and large in magnitude, and it is no longer possible to describe them using a constant value of the surface area adjustment factor F_A in the kinetic model of the hydrate formation/dissociation reaction. After appropriately modifying the T + H V1.5 code, we determined that the evolution of F_A over time is best described by a power equation $F_A = at^{-b}$ ($a,b > 0$) and we evaluated through the history-matching process the a and b parameters corresponding to the MH dissociation in the Chong et al. [19] experiment. Note that the shape and magnitude of the F_A equation during dissociation is substantially different from the time-dependent F_A for the hydrate formation experiments that was determined in the precursor study of Yin et al. [55].

5. During the early part of Step 3, the pressure difference ΔP between the reactor and the backpressure (i.e., the driving force of dissociation) is at a maximum, leading to rapid, high-rate dissociation that approaches equilibrium levels, as indicated by the very high value of F_A at this point (>100). During this step, dissociation is limited only by heat transport from the hydrate surroundings, i.e., the metal walls of the reactor and the circulating water bath at some locations.

6. As time advances in Step 3, the pressure difference ΔP decreases and the temperature decreases (because of the endothermic dissociation reaction), leading in a reduction in the rate of MH dissociation. This is attested to by the drastic decline in the value of F_A at these times. During this step, dissociation is kinetically retarded, despite the significant heat inflows from the boundaries that lead to localized temperature increases in their vicinity.

7. Under the conditions of the laboratory experiments of Chong et al. [19], kinetic retardation is far less significant during the MH dissociation process

($10^{-2} < F_A < 1\,0^{2}$) than during the MH formation process ($10^{-6} < F_A < 1\,0^{1}$) [55].

8. The inverse modelling (history-matching) process allowed the determination of the values of the dominant parameters (flow, thermal and kinetic) that control the system behaviour, yielding numerical simulation results that were in very good agreement with the experimental measurements, thus increasing confidence in the T + H V1.5 simulator.

Acknowledgement

The financial support from the National University of Singapore (R-261-508-001-646 and R-261-508-001-733) is greatly appreciated. Dr. George Moridis, the holder of the ExxonMobil Visiting Chair in the Department of Chemical and Biomolecular Engineering at NUS, extends his thanks to ExxonMobil and NUS for their support. Zhenyuan Yin would like to thank the LRSPL and EDB for the industrial postgraduate programme (IPP) scholarship.

References

[1] P. Englezos**Clathrate hydrates**

Ind Eng Chem Res, 32 (1993), pp. 1251-1274

[2] E.D. Sloan**Fundamental principles and applications of natural gas hydrates**

Nature, 426 (2003), pp. 353-363

[3] A.V. Milkov**Global estimates of hydrate-bound gas in marine sediments: how much is really out there?**

Earth Sci Rev, 66 (2004), pp. 183-197

[4] G.J. MacDonald**The future of methane as an energy resource**

Ann Rev Energy., 15 (1990), pp. 53-83

[5] R. Boswell, T.S. Collett**Current perspectives on gas hydrate resources**

Energy Environ Sci, 4 (2011), pp. 1206-1215

[6] Y.F. Makogon**Hydrates of Hydrocarbon**

PennWell Publishing Company, USA (1997)

[7] E.D. Sloan Jr., C.A. Koh**Clathrate hydrates of the natural gases**

(3rd ed.), CRC Press, Boca Raton, FL (2008)

[8] Z.R. Chong, S.H.B. Yang, P. Babu, P. Linga, X.-S. Li**Review of natural gas hydrates as an energy resource: prospects and challenges**

Appl Energy, 162 (2016), pp. 1633-1652

[9] Dallimore SR, Collett TS, Taylor AE, Uchida T, Weber M, Chandra A, et al. Scientific results from the Mallik 2002 gas hydrate production research well

program, Mackenzie Delta, northwest territories, Canada: Preface. Bulletin of the Geological Survey of Canada; 2005.

[10] Kurihara M, Funatsu K, Ouchi H, Sato A, Yasuda M, Yamamoto K, et al. Analysis of 2007/2008 JOGMEC/NRCAN/AURORA Mallik gas hydrate production test through numerical simulation. In: 7th International conference on gas hydrates. Edinburgh, UK; 2011.

[11] Schoderbek D, Farrell H, Hester K, Howard J, Raterman K, Silpngarmlert S, et al. ConocoPhillips gas hydrate production test final technical report. United States Department of Energy; 2013.

[12] Yamamoto K. Japan completes first offshore methane hydrate production test - methane successfully produced from deepwater hydrate layers. Fire in the Ice: Department of Energy, Office of Fossil Energy, National Energy Technology Laboratory; 2013. p. 1–2.

[13] D.G. Russell, J.H. Goodrich, G.E. Perry, J.F. Bruskotter**Methods for predicting gas well performance**

J Petrol Technol, 18 (1966), pp. 99-108

[14] G.J. Moridis, T.S. Collett, R. Boswell, M. Kurihara, M.T. Reagan, C. Koh, *et al.***Toward production from gas hydrates: current status, assessment of resources, and simulation-based evaluation of technology and potential**

SPE Reservoir Eval Eng, 12 (2009), pp. 745-771

[15] G.J. Moridis, T.S. Collett, M. Pooladi-Darvish, S.H. Hancock, J.C. Santamarina, R. Boswell, *et al.***Challenges, uncertainties, and issues facing gas production from gas-hydrate deposits**

SPE Reservoir Eval Eng, 14 (2011), pp. 76-112

[16] J.-C. Feng, Y. Wang, X.-S. Li, G. Li, Y. Zhang, Z.-Y. Chen**Effect of horizontal and vertical well patterns on methane hydrate dissociation behaviors in pilot-scale hydrate simulator**

Appl Energy, 145 (2015), pp. 69-79

[17] X.-S. Li, B. Yang, G. Li, B. Li, Y. Zhang, Z.-Y. Chen**Experimental study on gas production from methane hydrate in porous media by huff and puff method in Pilot-Scale Hydrate Simulator**

Fuel, 94 (2012), pp. 486-494

[18] X.-S. Li, Y. Zhang, G. Li, Z.-Y. Chen, H.-J. Wu**Experimental investigation into the production behavior of methane hydrate in porous sediment by depressurization with a novel three-dimensional cubic hydrate simulator**

Energy Fuels, 25 (2011), pp. 4497-4505

[19] Z.R. Chong, Z. Yin, J.H.C. Tan, P. Linga**Experimental investigations on energy recovery from water-saturated hydrate bearing sediments via depressurization approach**

Appl Energy, 204 (2017), pp. 1513-1525

[20] H.O. Kono, S. Narasimhan, F. Song, D.H. Smith**Synthesis of methane gas hydrate in porous sediments and its dissociation by depressurizing**

Powder Technol, 122 (2002), pp. 239-246

[21] P. Linga, C. Haligva, S.C. Nam, J.A. Ripmeester, P. Englezos**Recovery of methane from hydrate formed in a variable volume bed of silica sand particles**

Energy Fuels, 23 (2009), pp. 5508-5516

[22] S. Wang, M. Yang, P. Wang, Y. Zhao, Y. Song**In situ observation of methane hydrate dissociation under different backpressures**

Energy Fuels, 29 (2015), pp. 3251-3256

[23] M. Yang, Z. Fu, L. Jiang, Y. Song**Gas recovery from depressurized methane hydrate deposits with different water saturations**

Appl Energy, 187 (2017), pp. 180-188

[24] M. Yang, Z. Fu, Y. Zhao, L. Jiang, J. Zhao, Y. Song**Effect of depressurization pressure on methane recovery from hydrate–gas–water bearing sediments**

Fuel, 166 (2016), pp. 419-426

[25] K.A. Birkedal, C.M. Freeman, G.J. Moridis, A. Graue**Numerical predictions of experimentally observed methane hydrate dissociation and reformation in sandstone**

Energy Fuels, 28 (2014), pp. 5573-5586

[26] S.A. Bagherzadeh, I.L. Moudrakovski, J.A. Ripmeester, P. Englezos**Magnetic resonance imaging of gas hydrate formation in a bed of silica sand particles**

Energy Fuels, 25 (2011), pp. 3083-3092

[27] T.J. Kneafsey, G.J. Moridis**X-Ray computed tomography examination and comparison of gas hydrate dissociation in NGHP-01 expedition (India) and Mount Elbert (Alaska) sediment cores: Experimental observations and numerical modeling**

Mar Pet Geol, 58 (2014), pp. 526-539

[28] J.U.N. Mikami, Y. Masuda, T. Uchida, T. Satoh, H. Takeda**Dissociation of natural gas hydrates observed by X-ray CT scanner**

Ann NY Acad Sci, 912 (2000), pp. 1011-1020

[29] T. Uchida, S. Dallimore, J.U.N. Mikami**Occurrences of natural gas hydrates beneath the permafrost zone in Mackenzie delta: visual and X-ray CT imagery**

Ann NY Acad Sci, 912 (2000), pp. 1021-1033

[30] E.V.L. Rees, T.J. Kneafsey**Seol Y Methane hydrate distribution from prolonged and repeated formation in natural and compacted sand samples: X-Ray CT observations**

J Geol Res (2011)

[31] K. You, T.J. Kneafsey, P.B. Flemings, P. Polito, S.L. Bryant**Salinity-buffered methane hydrate formation and dissociation in gas-rich systems**

J Geophys Res Solid Earth, 120 (2015), pp. 643-661

[32] T.J. Kneafsey, L. Tomutsa, G.J. Moridis, Y. Seol, B.M. Freifeld, C.E. Taylor, *et al.***Methane hydrate formation and dissociation in a partially saturated core-scale sand sample**

J Petrol Sci Eng, 56 (2007), pp. 108-126

[33] T.J. Kneafsey, Y. Seol, A. Gupta, L. Tomutsa**Permeability of laboratory-formed methane-hydrate-bearing sand: measurements and observations using x-ray computed tomography**

SPE J, 16 (2011), pp. 78-94

[34] Tomutsa L, Freifeld B, Kneafsey TJ, Stern LA. X-ray computed tomography observation of methane hydrate dissociation. In: SPE gas technology symposium. Calgary, Alberta, Canada: Society of Petroleum Engineers; 2002.

[35] M. Priegnitz, J. Thaler, E. Spangenberg, J.M. Schicks, J. Schrötter, S. Abendroth**Characterizing electrical properties and permeability changes of hydrate bearing sediments using ERT data**

Geophys J Int, 202 (2015), pp. 1599-1612

[36] M. Priegnitz, J. Thaler, E. Spangenberg, C. Rücker, J.M. Schicks**A cylindrical electrical resistivity tomography array for three-dimensional monitoring of hydrate formation and dissociation**

Rev Sci Instrum, 84 (2013), p. 104502

[37] Masuda Y, Fujinaga Y, Naganawa S, Fujita K, Sato K, Hayashi Y. Modeling and experimental studies on dissociation of methane gas hydrates in berea sandstone cores. In: Proceedings of third international conference on gas hydrates. Salt Lake City, Utah, USA;1999.

[38] H.C. Kim, P.R. Bishnoi, R.A. Heidemann, S.S.H. Rizvi**Kinetics of methane hydrate decomposition**

Chem Eng Sci, 42 (1987), pp. 1645-1653

[39] K. Nazridoust, G. Ahmadi**Computational modeling of methane hydrate dissociation in a sandstone core**

Chem Eng Sci, 62 (2007), pp. 6155-6177

[40] H. Liang, Y. Song, Y. Chen**Numerical simulation for laboratory-scale methane hydrate dissociation by depressurization**

Energy Convers Manage, 51 (2010), pp. 1883-1890

[41] X. Ruan, Y. Song, H. Liang, M. Yang, B. Dou**Numerical simulation of the gas production behavior of hydrate dissociation by depressurization in hydrate-bearing porous medium**

Energy Fuels, 26 (2012), pp. 1681-1694

[42] L. Chen, H. Yamada, Y. Kanda, G. Lacaille, E. Shoji, J. Okajima, *et al.***Numerical analysis of core-scale methane hydrate dissociation dynamics and multiphase flow in porous media**

Chem Eng Sci, 153 (2016), pp. 221-235

[43] J.S. Hardwick, S.A. Mathias**Masuda's sandstone core hydrate dissociation experiment revisited**

Chem Eng Sci, 175 (2018), pp. 98-109

[44] Masuda YF, Naganawa S, Fujita K, Sato K, Hayashi Y. Modeling and experimental studies on dissociation of methane gas hydrates in Berea sandstone cores. In: The 3rd international conference on gas hydrates. Salt Lake City, Utah; 1999.

[45] B. Li, X.-S. Li, G. Li**Kinetic studies of methane hydrate formation in porous media based on experiments in a pilot-scale hydrate simulator and a new model**

Chem Eng Sci, 105 (2014), pp. 220-230

[46] B. Li, X.-S. Li, G. Li, Y. Wang, J.-C. Feng**Kinetic behaviors of methane hydrate formation in porous media in different hydrate deposits**

Ind Eng Chem Res, 53 (2014), pp. 5464-5474

[47] X. Sun, K.K. Mohanty**Kinetic simulation of methane hydrate formation and dissociation in porous MSedia**

Chem Eng Sci, 61 (2006), pp. 3476-3495

[48] G. Li, B. Li, X.-S. Li, Y. Zhang, Y. Wang**experimental and numerical studies on gas production from methane hydrate in porous media by depressurization in pilot-scale hydrate simulator**

Energy Fuels, 26 (2012), pp. 6300-6310

[49] B. Li, G. Li, X.-S. Li, Q.-P. Li, B. Yang, Y. Zhang, *et al.***Gas production from methane hydrate in a pilot-scale hydrate simulator using the huff and puff method by experimental and numerical studies**

Energy Fuels, 26 (2012), pp. 7183-7194

[50] J.-C. Feng, Y. Wang, X.-S. Li, G. Li, Y. Zhang**Three dimensional experimental and numerical investigations into hydrate dissociation in sandy reservoir with dual horizontal wells**

Energy, 90 (Part 1) (2015), pp. 836-845

[51] L.-G. Tang, X.-S. Li, Z.-P. Feng, G. Li, S.-S. Fan**Control mechanisms for gas hydrate production by depressurization in different scale hydrate reservoirs**

Energy Fuels, 21 (2007), pp. 227-233

[52] B.J. Anderson, M. Kurihara, M.D. White, G.J. Moridis, S.J. Wilson, M. Pooladi-Darvish, *et al.***Regional long-term production modeling from a single well test, mount Elbert gas hydrate stratigraphic test well, Alaska North Slope**

Mar Pet Geol, 28 (2011), pp. 493-501

[53] Z. Yin, G. Moridis, Z.R. Chong, H.K. Tan, P. Linga**Numerical analysis of experiments on thermally induced dissociation of methane hydrates in porous media**

Ind Eng Chem Res, 57 (2018), pp. 5776-5791

[54] Z.R. Chong, G.A. Pujar, M. Yang, P. Linga**Methane hydrate formation in excess water simulating marine locations and the impact of thermal stimulation on energy recovery**

Appl Energy, 177 (2016), pp. 409-421

[55] Z. Yin, G. Moridis, H.K. Tan, P. Linga**Numerical analysis of experimental studies of methane hydrate formation in a sandy porous medium**

Appl Energy, 220 (2018), pp. 681-704

[56] M. Clarke, P.R. Bishnoi**Determination of the activation energy and intrinsic rate constant of methane gas hydrate decomposition**

Can J Chem Eng, 79 (2001), pp. 143-147

[57] Moridis GJ. User's manual for the hydrate v1. 5 option of TOUGH+ v1. 5: a code for the simulation of system behavior in hydrate-bearing geologic media. LBNL-6869E. Berkeley, California, USA: Lawrence Berkeley National Laboratory; 2014.

[58] Moridis G. User's manual of the TOUGH+ Core Code v1.5: a general-purpose simulator of non-isothermal flow and transport through porous and fractured media. LBNL-6871E. Berkeley, California, USA: Lawrence Berkeley National Laboratory; 2014.

[59] Moridis G. User’s manual of the MeshMaker v1. 5 code: a mesh generator for domain discretization in simulations of the TOUGH+ and

TOUGH2 families of codes. LBNL 1005134. Berkeley, California, USA: Lawrence Berkeley National Laboratory; 2016.

[60] G. Moridis**Numerical studies of gas production from methane hydrates**

SPE J, 8 (2003), pp. 359-370

[61] G. Moridis, M. Kowalsky

Gas production from unconfined class 2 oceanic hydrate accumulations. Economic geology of natural gas hydrate, Springer, Netherlands (2006), pp. 249-266

[62] Moridis G, Collett T. Strategies for gas production from hydrate accumulations under various geologic conditions. Report LBNL-52568. Berkeley, California: Lawrence Berkeley National Laboratory; 2003.

[63] G.J. Moridis, T.S. Collett, S.R. Dallimore, T. Satoh, S. Hancock, B. Weatherill**Numerical studies of gas production from several CH_4 hydrate zones at the Mallik Site, Mackenzie Delta, Canada**

J Petrol Sci Eng, 43 (2004), pp. 219-238

[64] G.J. Moridis, J. Kim, M.T. Reagan, S.-J. Kim**Feasibility of gas production from a gas hydrate accumulation at the UBGH2-6 site of the Ulleung Basin in the Korean East Sea**

J Petrol Sci Eng, 108S (2013), pp. 180-210

[65] G.J. Moridis, M.B. Kowalsky, K. Pruess**Depressurization-induced gas production from Class-1 hydrate deposits**

SPE Reservoir Eval Eng, 10 (2007), pp. 458-481

[66] Moridis GJ, Reagan MT. Strategies for gas production from oceanic class 3 hydrate accumulations. In: Offshore technology conference. Houston, Texas: Offshore Technology Conference; 2007.

[67] H. Stone**Probability model for estimating three-phase relative permeability**

J Petrol Technol, 22 (1970), pp. 214-218

[68] M.T. Van Genuchten**A closed-form equation for predicting the hydraulic conductivity of unsaturated soils**

Soil Sci Soc Am J, 44 (1980), pp. 892-898

[69] B. Ghanbarian-Alavijeh, A. Liaghat, G.-H. Huang, M.T. Van Genuchten**Estimation of the van Genuchten soil water retention properties from soil textural data**

Pedosphere, 20 (2010), pp. 456-465

[70] L.K. Thomas, L. Hellums, G. Reheis**A nonlinear automatic history matching technique for reservoir simulation models**

Soc Petrol Eng J, 12 (1972), pp. 508-514

[71] M.B. Kowalsky, G.J. Moridis**Comparison of kinetic and equilibrium reaction models in simulating gas hydrate behavior in porous media**

Energy Convers Manage, 48 (2007), pp. 1850-1863

[72] A. Gupta, S.F. Dec, C.A. Koh, E.D. Sloan**NMR Investigation of methane hydrate dissociation**

J Phys Chem C, 111 (2007), pp. 2341-2346

[73] S. Subramanian, E.D. Sloan**Molecular measurements of methane hydrate formation**

Fluid Phase Equilib, 158–160 (1999), pp. 813-820

[74] Kurihara M, Sato A, Funatsu K, Ouchi H, Yamamoto K, Numasawa M, et al. Analysis of production data for 2007/2008 Mallik gas hydrate production tests in Canada. In: International oil and gas conference and exhibition in China. Beijing, China: Society of Petroleum Engineers; 2010.

[75] A. Oyama, S. Masutani**A Review of the methane hydrate program in japan**

Energies, 10 (2017), p. 1447

[76] Xinhua. China wraps up combustible ice mining trial, setting world records. Guang Zhou; 2017.